

Original Article



Journal of Cerebral Blood Flow & Metabolism I–12 © The Author(s) 2025 Article reuse guidelines: sagepub.com/journals-permissions DOI: 10.1177/0271678X251386182 journals.sagepub.com/home/jcbfm



Comparison of approaches for surface vessel diameter and pulsatility quantification

Aditya Ranjan¹, Devin T Wong², Qinwen Huang³, Hashmat Ghanizada^{4,5}, Maiken Nedergaard^{3,5}, Douglas H Kelley¹ and Kimberly A S Boster¹

Abstract

Cerebral blood vessels change diameter with each heartbeat, in response to oxygen demand, and during pathological states. To study these dynamics, vessel diameters are often quantified from intravital microscope images. We compare three different image-based vessel diameter measurement algorithms: one that uses an intensity threshold (cross section threshold (CST)), one that performs a Radon transform then calculates its full width at half maximum (FWHM), and a newly developed algorithm that leverages the intensity gradient (find image edges (FIE)). Using synthetic data, we find that the average errors in FIE, CST, and FWHM are 3.7%, 2.4%, and 0.2%, respectively, for images with a low noise-to-signal ratio (NSR = 0.07). Of the three, FIE best maintains accuracy for images with larger NSR and brightness gradients, though a modification to FWHM allows it to maintain accuracy with larger NSR. We also introduce a novel approach to quantify the vessel pulsation amplitude based on the interquartile range (IQR) and find it to be as accurate as an existing method, phase averaging (PA). FIE is best for measuring relative changes in vessel diameter and the average diameter in the presence of noise or other lighting artifacts, and FWHM is best for measuring the average diameter.

Keywords

Vessel diameter, Radon transform, full width at half maximum, vessel pulsation, image analysis

Received 15 March 2025; Revised 29 July 2025; Accepted 18 September 2025

Introduction

Pial arteries supply blood to the cerebral cortex, forming a network on the cortical surface which connects the major cerebral arteries to the cortical arterioles. Pial arteries range in diameter from 50 to 280 µm in humans. Under prehypoxia baseline conditions, the diameters of pial arteries and penetrating arterioles in mice are $34 \pm 8 \,\mu m$ (mean \pm standard deviation) and $17 \pm 5 \,\mu m$, respectively.² However, their diameters are dynamic. Cerebral vessels change size in synchrony with the cardiac cycle³ and at lower frequencies (slow vasomotion⁴), including in response to changes in metabolic demand for blood (i.e. functional hyperemia⁵⁻⁷) or in response to trauma. For instance, a reduction in vessel diameter by more than 50% has been observed in vasospasm after aneurysmal subarachnoid hemorrhage.8 Diameter fluctuations affect cerebral blood flow and can lead to ischemia or hyperemia. Diameter fluctuations also drive flow of cerebrospinal fluid (CSF) in adjacent perivascular spaces (PVSs),4,9,10 with implications for clearance of brain wastes. 11,12 Therefore, vessel diameter changes can be an important indicator of pathological and physiological conditions.

Department of Mechanical Engineering, University of Rochester, Rochester, NY, USA

²Department of Biomedical Engineering, University of Rochester,

Rochester, NY, USA

³Division of Glial Disease and Therapeutics, Center for Translational Neuromedicine, University of Rochester, Rochester, NY, USA

⁴Department of Neurology and Danish Headache Center, Rigshospitalet Glostrup, Faculty of Health and Medical Sciences,

University of Copenhagen, Copenhagen, Denmark ⁵Center for Translational Neuromedicine, University of Copenhagen, Copenhagen, Denmark

Corresponding author:

Kimberly A S Boster, Department of Mechanical Engineering, University of Rochester, 235 Hopeman Engineering Building, Rochester, NY 14627-0132, USA.

Email: kboster@ur.rochester.edu

Various diameter measurement approaches have been used previously. A basic approach is manually measuring the diameter from an image, but manual approaches are time-consuming and prone to error. 13 Lee et al. presented an automated feature-based tracking algorithm for measuring the diameter in intravital microscopic videos. 13 For regions larger than 69 µm, the average error was under 0.1 µm. However, for smaller regions (such as 17 µm) the error was larger, indicating that not enough features were captured. Also, the algorithm was unable to capture the vessel wall when it was blurry. An experimental photoacoustic imaging technique involved delivering laser pulses to vessels to induce a pressure transient and create acoustic waves to be detected by double ring sensors. The vessel diameter was approximated using a mathematical model relating the vessel diameter to the pressure wave's period, the speed of sound in blood, and the laser pulse duration. However, this technique was unable to measure large vessel diameters (>1.2 mm) due to the frequency response of the system. 14

Another common approach for an image showing a bright vessel with dark surroundings is to take the vessel width to be the distance, along a vessel cross section, between the two innermost locations where brightness is less than half the maximum brightness—the full width, at half the maximum. Fischer et al. used a custom ImageJ plugin based on this approach.¹⁵ Baran et al. applied it to optical microangiography, a label-free imaging technique. 16 Will et al. found better accuracy with this approach when the reference intensity was chosen to be the median intensity outside the blood vessel.¹⁷ Glück et al. fitted Gaussian intensity profiles to vessel images, then determined the widths of those fits. 18 Applying the approach to a Radon transformation of the vessel image, not the image itself, usually produces superior results because it uses the entire region of interest (ROI), rather than a single line.¹⁹

We developed a new method for determining vessel diameters using gradient-based edge detection, which we call "find image edges" (FIE). In this work, we compare the performance of FIE, a Radon transform-based full width at half maximum algorithm¹⁹ (FWHM), and an algorithm that locates vessel edges using an intensity threshold,²⁰ here called "cross section threshold" (CST).

This paper is structured as follows. First, we explain the algorithms for determining diameters. Then, we describe two different methods to quantify vessel pulsatility. Next, we use those methods to compare diameter estimates produced by the three algorithms, for synthetic data (where the ground-truth diameter is known) and experimental data.

Materials and methods

Find image edges (FIE)

We developed an algorithm for measuring diameter, "find image edges" (FIE), that locates vessel edges at places of steepest intensity gradients, using MATLAB's edge-finding algorithm, which uses the Canny method^{21–23} by default. The algorithm first detects edges in each frame, and optionally applies a user-defined mask (the same mask for the entire video) to eliminate non-vessel edges. If not defined by the user, FIE automatically generates the mask based on average edges and allows the user to perform further refinement. The mask is then dilated to ensure that the vessel edge lies within the mask boundaries. The user draws "end caps" perpendicular to the vessel axis to enclose a region, which is filled in to segment the vessel as illustrated in Figure 1(a). The diameter is evaluated by dividing the area of the segmented region by the distance between the end caps. The visual output from FIE is illustrated in Supplementary Figure S1(b).

Cross section threshold (CST)

The "cross section threshold" (CST) algorithm²⁰ locates points on vessel edges as places on vessel cross sections where brightness drops below a user-specified threshold (given as a fraction of maximum brightness). The user also marks the vessel centerline, sets the ROI, and specifies the number of (equally-spaced) vessel cross sections. Figure 1(b) shows an example. The median diameter across all cross-sections is computed for each frame. The visual output from CST is illustrated in Supplementary Figure S1(a).

Full width at half maximum (FWHM)

The FWHM algorithm is described by Huo et al. 19,24 and uses the full-width half-max approach on the Radon transformation of an image (Figure 1(c)) to calculate the vessel diameter. The key user inputs are the centerline and the ROI. The first step in the algorithm is to correct motion artifacts by registering the images (with respect to the first frame) via cross-correlation on the two-dimensional discrete Fourier transform of the images and applying translations in the real domain. Then, a Radon transform is applied in the direction of the centerline, effectively averaging the intensity in that direction to generate a projection profile. A one-dimensional median filter (with a 5-pixel window) is applied to smooth the profile. The vessel diameter is defined as the width of the region where the profile exceeds its minimum value by at least half the maximum. Linear interpolation is used to determine the width with sub-pixel accuracy. 19,24

Synthetic data generation

We generated synthetic images that mimic pulsing vessels using custom MATLAB code (Figure 2(a)). We used a frame rate of 30 Hz and a 4-Hz (sinusoidal) pulsation frequency, typical of the heart rate of an anesthetized mouse. The mean vessel diameter was 40 pixels and the image

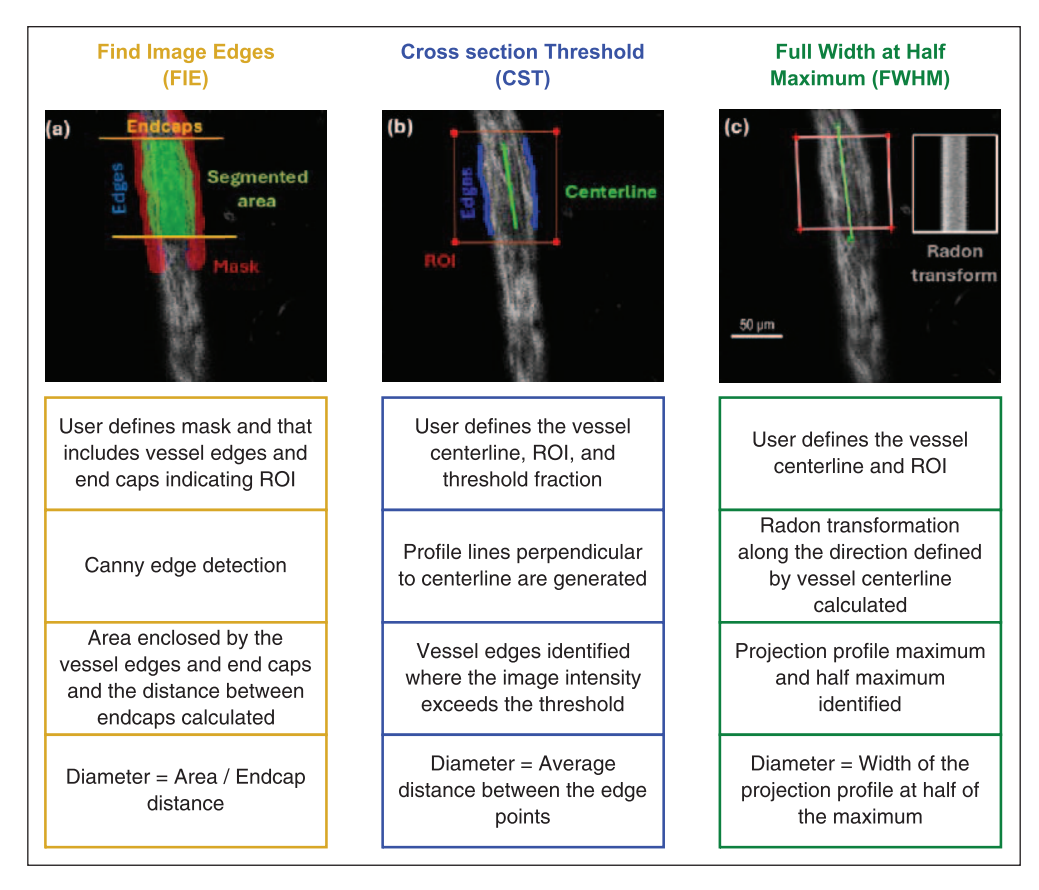


Figure 1. Flowchart describing the different vessel diameter measurement algorithms. (a) FIE, (b) CST, (c) FWHM. Panel (a) shows the segmented area (green) confined between the vessel edges (blue) and the end caps (yellow line). The mask is shown in red. The ROI and centerline are indicated with a red box and green line, respectively, in panels (b) and (c). The inset in panel (c) shows the projected intensity profile for several frames.

FIE: find image edges; CST: cross section threshold; FWHM: full width at half maximum.

was 100×100 pixels. We varied the radial pulsation amplitude from 0.2 to 2 pixels, using 1 pixel unless otherwise stated. The images were blurred using the built-in MATLAB function imgaussfilt with a standard deviation of 1 pixel. We added random noise to each frame, such that the noise-to-signal ratio (NSR) varied from 0 to 2.26 (inset in Figure 3(d) and (g)); unless otherwise noted, the NSR is 0.07.

We also generated synthetic images where the diameter varied axially with an amplitude of 1 pixel and wave number 0.05 radians/pixel (Figure 2(b)). We generated other synthetic images with a curved vessel (Figure 2(c)). Specifically, the centerline was modified into a parabolic shape by introducing a displacement in the y direction that was proportional to the square of the relative x distance from the midpoint with a displacement factor A = 10.

For each synthetic image, we calculated the noise-tosignal ratio (NSR) by dividing the mean of the square of the noise added to the image array by the signal intensity squared:

$$NSR = \frac{1}{S^2} \frac{1}{T} \sum_{t=1}^{T} N_t^2$$
 (1)

where S is the intensity of the vessel (S=1 in all synthetic data), N_t is the difference between the intensity of the tth pixel before and after adding noise, and T is the total number of pixels in time and space.

To mimic motion artifacts in real vessel diameter measurements, we varied the vessel position by shifting the images in a direction perpendicular to the vessel by a distance that varied sinusoidally with 4-Hz frequency and with an amplitude between 0 and 9 pixels.

To mimic uneven illumination, we added an image-wide brightness gradient with slope 0.01 (on a 0–1 brightness scale)/pixel and one of three orientations: parallel to the vessel (inset in Figure 3(i)), perpendicular to the vessel (inset in Figure 3(f)), or at a 45° angle to the vessel.

To mimic unsteady illumination, we added a fixed brightness increment (0.01) to all pixels for 10 consecutive frames, starting at a randomly selected frame.

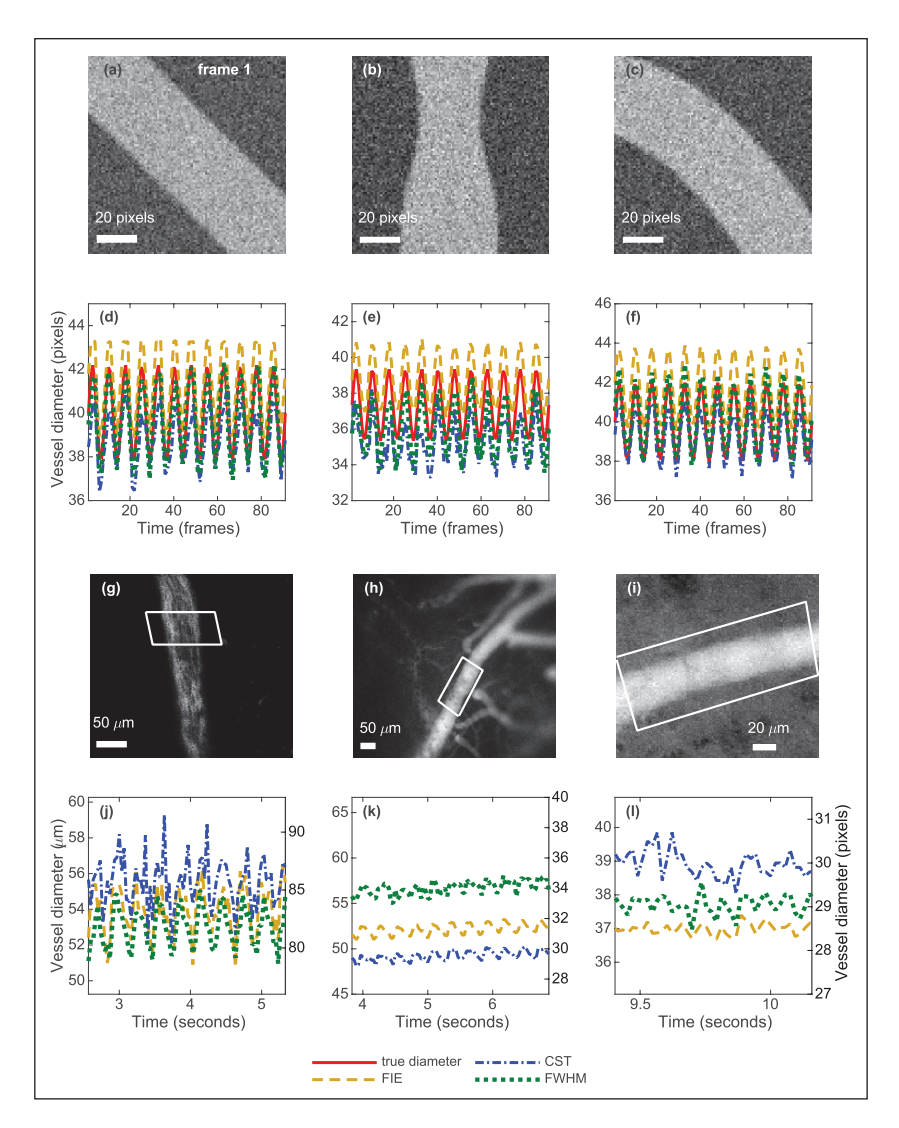


Figure 2. Representative images and diameter measurements from the different algorithms for a synthetic straight vessel (a, d), a synthetic vessel with diameter variation (b, e), a synthetic vessel with curvature (c, f), and experimental data (g–l), including two-photon microscopy through a cranial window (ROI indicated with a white box) (g, j), fluorescence microscopy through a thinned skull (h, k), and macroscopic imaging of an awake mouse through an intact skull (i, l).

In vivo image collection

We analyzed three time-series of images acquired using three different imaging modalities. The reporting of animal experiments in this manuscript follows the ARRIVE guidelines 2.0.²⁵ First, for the publicly available data²⁶ shown in Figure 2(g), wild-type mice were anesthetized using ketamine/xylazine, and cranial windows were installed. The mice received an intravenous injection of FITC-conjugated dextran (2000 kDa) to visualize the blood vessel lumen as described in Boster et al.²⁷ The two-photon images were acquired at 30 frames/s with a spatial resolution of 0.648 microns/pixel.

For the newly acquired data shown in Figure 2(h), the mouse skull was thinned at the area of the middle cerebral artery (MCA) and fitted with a head plate. The mouse was

allowed to recover from the surgery for 1 week. Before the imaging, the mouse was anesthetized with ketamine and xylazine cocktail (80 and 10 mg/kg), then retroorbital injected with fluorescent tracer (0.1 ml, 1%, albumin from bovine serum 647; Thermo Fisher Scientific catalog: A34785). The mouse was head fixed and carefully monitored to be deeply anesthetized during the imaging. Branches of the MCA were identified. Videos of the artery were recorded at 30 frames/s, with a spatial resolution of 0.6 pixel/micron, using a stereo microscope (Leica M205FA) with a CMOS camera (Hamamatsu, ORCA-Flash4.0) and $1 \times$ Leica objective (part number: 10450028). All experiments were conducted in strict accordance with the Guide for the Care and Use of Laboratory Animals and were approved by the University Committee on Animal Resources (UCAR), University of Rochester Medical

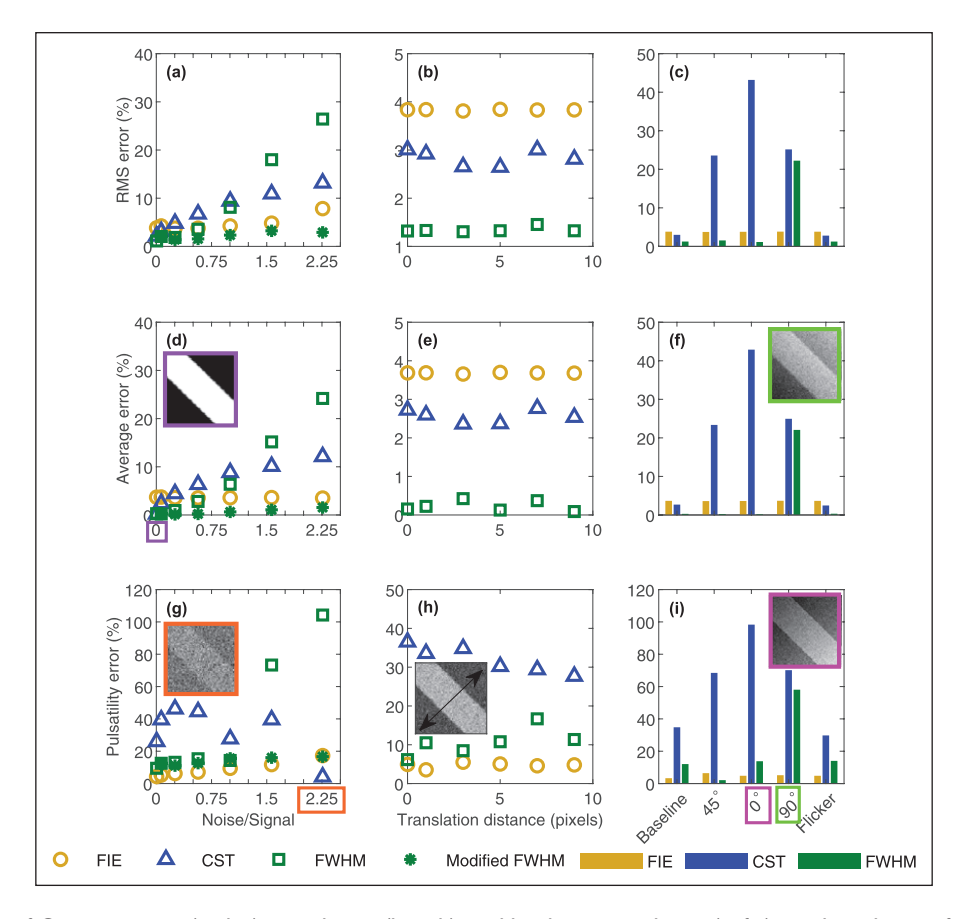


Figure 3. Effect of Gaussian noise (a, d, g), translation (b, e, h), and brightness gradients (c, f, i) on algorithm performance. Gradients were applied either parallel or perpendicular to the synthetic vessel. Pulsatility error was obtained using the IQR approach.

RMS: root-mean-square.

Center certified by Association for Assessment and Accreditation of Laboratory Animal Care.

For the newly acquired data shown in Figure 2(i), a wild-type mouse skull was thinned at the area of the MCA and fitted with a head plate for fixation. The mouse was allowed to recover from the surgery for 1 week and was habituated for awake imaging. The mouse was head-fixed on a physiological monitoring system (Small Animal Physiological Monitoring system, 75–1500; Harvard Apparatus), and temperature, electrocardiogram (ECG), and respiration rate were monitored. A wide-field brightlight macroscope (Leica, M205 FA) with CMOS camera (Hamamatsu, Orca-Flash 4.0, C11440) was used for imaging. A branch of the MCA was identified and a region of interest (ROI) chosen for continuous imaging. The spatial and temporal resolution were 1.29 microns/pixel and 54.47 frames/s, respectively. All experiments were conducted in strict accordance with the Institutional Animal Care and Use Committee (IACUC) at the University of Copenhagen and all animal procedures were approved by the Office of Laboratory Animal Welfare (OLAW) and conducted in accordance with the Association for Assessment and Accreditation of Laboratory Animal Care.

The three different in vivo datasets shown in Figure 2 represent different imaging approaches with varying levels of imaging quality. The images in Figure 2(g) and (h) show fluorescent tracers injected into the blood to mark the vessel. In Figure 2(g), the vessel was visualized through a cranial window, which leads to superior image quality but is more invasive, whereas in Figure 2(h), the vessel was visualized through a thinned skull, reducing the image quality but being less invasive. In Figure 2(i), the vessel was illuminated using a bright light and visualized through a thinned skull, leading to the lowest quality imaging but least invasive procedure. Two-photon microscopy generally allows for higher resolution imaging compared to macroscopy.

Pulsatility metrics

The amplitude of vessel pulsation has important implications for both cerebral blood flow and CSF flow in PVSs adjacent to blood vessels, and we will refer to this quantity as the vessel pulsatility. One way to determine the pulsatility is by phase-averaging (PA), where the vessel diameters from many cycles are averaged together to yield the

Cutoff frequency (Hz)	Ground truth amplitude	IQR/ $\sqrt{2}$ (% error)		
		B=0	B = 1	B=2
3–8	1.00	0.99 (0.00)	0.97 (2.95)	1.34 (34.38)
0.03-0.5	3.00	3.00 (0.00)	2.99 (0.34)	2.95 (1.74)
1/70-1/30	2.00	2 (0.00)	1.99 (0.00)	1.99 (0.21)

Table 1. Comparison of ground-truth amplitudes and amplitudes estimated using the IQR metric. Percent error is indicated in parentheses.

evolution of the diameter over an idealized pulsation cycle, and the amplitude is defined as half of the difference between the maximum and minimum of the PA waveform. However, PA assumes a periodic oscillation of known frequency. Because real vessels pulse aperiodically, we also present and compare an alternative approach based on the interquartile range of the vessel diameter.

Phase averaging (PA). PA has been used previously to quantify vessel pulsation. Assuming pulsation is cyclical (e.g. with cardiac activity), PA starts by binning diameter measurements according to the fraction of the cycle at which each measurement was made, then averages all measurements in each bin, producing a waveform that shows how diameter is expected to vary throughout the cycle. By combining measurements from many cycles, PA reduces noise and effectively increases the sampling frequency. For example, if the sampling frequency is 30 Hz and the pulsation frequency is 4 Hz, only seven or eight measurements are made in each cycle, hindering calculation of the vessel wall speed from numerical differentiation. But with PA, many more measurements of the wall position over the cycle can be combined (often 50 or 100). Using this approach requires knowing when each cycle begins, for instance, via ECG measurements of the cardiac cycle.

Interquartile range (IQR). We devised an alternative for quantifying the pulsatility: the IQR method. IQR is defined as the difference between the 75th and 25th percentiles of a dataset. It is particularly useful for cardiac pulsatility when ECG measurements are unavailable, or for slow vasomotion, which lacks a periodic cycle. For a sine wave, IQR and amplitude are related by a factor of $\sqrt{2}$, as shown in the Supplementary Material, so in order to compare with the amplitude obtained from PA, we divide the IQR by $\sqrt{2}$. The IQR approach provides no information on the waveform shape or wall speed.

To validate the IQR approach, we generated synthetic, time-varying diameters that contained three different frequency components, as might arise from cardiac pulsations (f_1) , respiration (f_2) , and slow vasomotion (f_3) :

$$y = A_0 + A_1 \sin(2\pi f_1 t) + A_2 \sin(2\pi f_2 t) + A_3 \sin(2\pi f_3 t) + B\eta(t)$$
(2)

Here, $A_0 = 20$, f_1 varies over time from 6 to 7 Hz, $A_1 = 1$, $f_2 = 0.25 \,\text{Hz}, A_2 = 3, f_3 = 0.02 \,\text{Hz}, A_3 = 2, t \text{ is time, } \eta (t) \text{ is a}$ series of values sampled from the standard normal distribution, and B is either 1 or 2 so that the standard deviation of the noise term is either 1 or 2. The resulting signal was sampled at 30 Hz. We subtracted the temporal mean diameter and applied a bandpass filter with 60 dB attenuation in the stopband. (We did not filter synthetic data, in which only a single frequency was present before noise was applied.) The bandpass filter uses cutoff frequencies (listed in Table 1) that include the single frequency signal of interest. We calculated the IQR (the difference between the 75th and 25th percentiles) of the filtered diameter measurements. Then, we compared the amplitude of the synthetic signals calculated using the IQR approach to the ground-truth amplitude, as shown in Table 1. Supplementary Figure S2 graphically illustrates the validation process. Briefly, the sum of three single-frequency signals was corrupted with Gaussian noise and subjected to a filter with a passband around the first frequency, and the IQR/ $\sqrt{2}$ of the result was compared to the amplitude of the first single-frequency signal (see Supplementary Figure S2). The process was repeated for the second and third frequencies.

Error metrics

We used four error metrics: average error, root-meansquare (RMS) error, IQR pulsatility error, and PA pulsatility error, to compare measurements to ground-truth data. Given a collection of n images, if the ground-truth vessel diameter in image i is $d_{i,GT}$ and the measured diameter in the same image is d_i A, then the average error is defined as:

Average error =
$$\frac{1}{n} \sum_{i=1}^{n} \left(\frac{d_{i,GT} - d_{i,A}}{d_{i,GT}} \right)$$
 (3)

and the RMS error is defined as:

RMS error =
$$\sqrt{\frac{1}{n} \sum_{i=1}^{n} \left(\frac{d_{i,GT} - d_{i,A}}{d_{i,GT}} \right)^2}$$
 (4)

Across a collection of images, the diameter of a pulsing vessel fluctuates around its mean value. If the IQR of the ground-truth vessel diameter fluctuation is IQR_{GT} and the IQR of the measured diameter fluctuation is IQR_A , then the IQR pulsatility error is defined as:

$$IQR \text{ pulsatility error} = \left| \frac{IQR_{GT} - IQR_{A}}{IQR_{GT}} \right|$$
 (5)

The PA amplitude is defined as half the difference between the minimum and maximum values of a PA vessel diameter profile. If the PA amplitude of the ground-truth vessel diameter is PA_{GT} and the PA amplitude of the measured diameter is PA, the PA pulsatility error is defined as:

$$PA \text{ pulsatility error} = \left| \frac{PA_{GT} - PA_{A}}{PA_{GT}} \right|$$
 (6)

The random noise included in our synthetic data caused error metrics to vary in repeated trials. We chose the frame count n large enough that variations were no >5%: $n \ge 45$ for average and RMS errors, and typically $n \approx 10^6$ for pulsatility errors (Supplementary Figure S3).

Results

Quantifying pulsatility in synthetic and experimental data

Figure 2(a) shows a representative synthetic vessel image, and Figure 2(d) shows the variation of vessel diameter over a series of such images. The ground-truth diameter used to construct the synthetic images is shown along with the measurements made using each of the three algorithms (FIE, CST, and FWHM). FIE exhibits 3.7% average error, 4.2% RMS error, and 5.3% pulsatility error using the IQR approach. In this example, FIE overestimates the average diameter because the vessel edge detected by the Canny method includes pixels outside the vessel, which are counted in the total vessel area, as illustrated in Supplementary Figure S4. Having a portion of the edge outside the vessel only affects absolute vessel measurements and does not affect the pulsatility measurement or any relative measure of vessel diameter change. CST underestimates the diameter for the threshold used here (0.5), average, RMS, and pulsatility errors of 2.4%, 3.1%, and 39.4%, respectively. CST is sensitive to the threshold. The average error is reduced to 0.3% from 2.7% when using a threshold of 0.45. With a still lower threshold (<0.45), CST overestimates the diameter. The waveform generated by FWHM is closest to capturing the true waveform, with average, RMS, and pulsatility errors of 0.2%, 2.1%, and 12.5%, respectively.

The performance of the three algorithms on vessels with axial diameter variation (Figure 2(b) and (e)) and curved vessels (Figure 2(c) and (f)) was similar to their performance on straight vessels. For vessels with axial diameter variation (Figure 2(b)), FIE resulted in average and RMS errors of 3.9%, with the smallest pulsatility error (6.7%) of the three algorithms. CST had the highest error for all three types of error, with average, RMS, and pulsatility errors of 5.6%, 5.9%, and 38.6%, respectively. FWHM demonstrated the lowest average and RMS errors (3.4% and 3.7%) while the pulsatility error was 11.9%. Similarly, for synthetic data with parabolic curvature (Figure 2(c)), FIE exhibited average and RMS errors of 4.5% and pulsatility error of 4.1%. CST showed slightly lower average error (1.8%) and RMS error (2.2%); however, the pulsatility error (31.4%) was the highest among the three algorithms. FWHM achieved the lowest error in absolute diameter measurement, with 0.6% average error and 1.1% RMS error. However, the pulsatility error was 10.9%.

Figure 2(g)-(i) show representative images recorded in vivo using a two-photon microscope through a cranial window, a fluorescence microscope through a thinned skull, and a bright light macroscope through a thinned skull, respectively. Figure 2(j) shows diameter measurements from a series of two-photon images, which have high resolution and appear to have low NSR. The three algorithms perform similarly, though FIE and FWHM match each other more closely than CST matches either. The mean diameters for the twophoton microscopy data from FIE, CST, and FWHM were 53.4, 55.3, and 53.0 µm, respectively. The pulsation amplitudes obtained using the IQR approach from FIE, CST, and FWHM were 1.6, 1.2, and 1.2 μm, respectively. The similarity in pulsatility measurements suggests that any of the three approaches would work reasonably well for measuring pulsatility for this type of imaging. For the fluorescence microscope data shown in Figure 2(h), the mean diameters from FIE, CST, and FWHM were 51.8, 48.7, and 56.5 μm, respectively. The amplitudes obtained from FIE, CST, and FWHM were 0.86, 0.56, and 0.70 µm, respectively. For the macroscope data shown in Figure 2(i), the mean diameters from FIE, CST, and FWHM were 36.8, 38.6, and 37.5 µm, respectively. However, the difference in pulsation amplitude between algorithms is larger (0.18, 0.23, and 0.29 µm from FIE, CST, and FWHM, respectively), but since we do not have ground-truth measurements, we cannot necessarily say which algorithm is best. For the thinned skull fluorescence microscopy and bright light macroscopy images (Figure 2(h) and (i)), we observe more significant differences from one algorithm to another (Figure 2(k) and (l)). The mean diameter values measured using the three algorithms suggest that each algorithm demonstrates potential suitability to estimate the mean diameter of vessels accurately.

Robustness to imaging artifacts

Next, we sought to quantify the robustness of each algorithm to varying NSR, translation, and brightness by adding artifacts to a synthetic image of a straight vessel like the one shown in Figure 2(a). Figure 3(a), (d), and (g) show the effects of noise. The insets in Figure 3(d) and (g) show frames with NSR of 0 and 2.26, respectively. We used the IQR approach to measure the pulsatility error caused by the artifacts introduced in the synthetic data discussed in Figure 3. For NSR of 0, the RMS errors for FIE, CST, and FWHM are 3.8%, 2.1%, and 1.1%, respectively. The average errors are 3.7%, 0.2%, and 0.3%, respectively. For noiseless images, FWHM performs best and FIE performs worst because the algorithm erroneously includes some edge pixels. The pulsatility errors are 4.4%, 25.9%, and 9.4%, respectively. The RMS and average errors increase with NSR for every algorithm, but the rate of increase is much lower for FIE, indicating that it is much less sensitive to noise. For NSR of 1, the RMS errors for FIE, CST, and FWHM are 4.2%, 9.4%, and 8.1%, respectively, and the average errors are 3.6%, 8.8%, and 6.4%, respectively. At NSR 1, the pulsatility errors are 9.4%, 27.7%, and 14.3% for FIE, CST, and FWHM, respectively.

For NSR ≥1, the FWHM algorithm resulted in significantly higher errors in absolute diameter and pulsatility measurements. We investigated the source of the high error in FWHM and found at high levels of noise, the background intensity was much larger than zero, so the algorithm often incorrectly identified the edge of the ROI as the vessel edge (Supplementary Figure S5(a) and (b)). To improve the performance of FWHM with noisy data, we made two modifications to the algorithm. First, the original FWHM algorithm places vessel edges where the value of the Radon-transformed intensity profile is half the maximum value. In the case of a noisy image (or one where the background intensity is non-zero, even if there is adequate contrast between the vessel and background), the maximum is not a good representation of the difference between the vessel and background. The vessel diameter is overestimated, and if the background intensity exceeds half the maximum value, vessel edges are located at the edge of the ROI, rather than the edge of the vessel.

We overcame this drawback by placing vessel edges where the intensity value falls halfway between the maximum value (to represent the vessel intensity) and the 10th percentile of the nonzero intensity values (to represent the background intensity, instead of the minimum intensity). For an NSR of 2.26, the original algorithm (FWHM) resulted in average, RMS, and pulsatility errors of 24.2%, 26.4%, and 104.3%, respectively. For noisy data, it is more appropriate to use half of the difference between the background and vessel intensities. With the redefined baseline measurement, the errors dropped to 0.9%, 3.8%, and 15.2%, respectively ("Modified with registration" in Supplementary Figure S6). Supplementary Figure S5(c)

compares the results of FWHM and modified FWHM with the true diameter measurements for NSR of 2.26.

Second, the original FWHM algorithm applies a DFT-based image registration. At high NSR, it applies large registration shifts where it should not. For images with no or little translation (such as our synthetic data) and substantial noise, eliminating DFT registration enhanced the performance of the FWHM algorithm. When we eliminated DFT registration and used the 10th-percentile baseline (an algorithm we call "Modified FWHM"), the average, RMS, and pulsatility errors changed from 24.2% to 1.5%, 26.4% to 2.9%, and 104.3% to 16.6%, respectively for NSR=2.26 (Figure 3(a), (d), and (g) and Supplementary Figure S6). For low-noise images, performance was not appreciably affected by retaining or eliminating DFT image registration.

To explore the impact of microscope or vessel movement during image acquisition, we investigated the effect of displacing the vessel perpendicular to its edge (Figure 3(b), (e), and (h)). The inset in Figure 3(h) shows the direction of vessel translation. None of the algorithms are sensitive to displacements smaller than 10 pixels for the synthetic data we tested.

We also quantified the algorithms' performance in the presence of brightness gradients parallel to the vessel (0° angle), perpendicular to the vessel (90° angle), and at a 45° angle with the vessel (Figure 3(c), (f), and (i)). CST is highly sensitive to brightness gradients in all three directions. When brightness varies spatially, a single threshold value cannot accurately locate the vessel edges. FWHM is sensitive to a brightness gradient imposed perpendicular to the vessel if the resulting background intensity on one side of the vessel substantially exceeds the 10th percentile, as shown in Supplementary Figure S7. In that case, the algorithm places the corresponding vessel edge erroneously far from the vessel center (sometimes at the edge of the ROI), overestimating the diameter. Our modifications to FWHM do not improve its robustness to brightness gradients. In contrast, FIE is robust to brightness gradients since it places vessel edges based only on local intensity variations rather than intensity magnitude.

"Flicker," or spatially uniform but temporally random brightness variations, had little effect (Figure 3(c), (f), and (i)).

Sensitivity to user inputs

All of the algorithms require user inputs that can affect results. For CST, Figure 4(a) illustrates the variation of the average error as a function of the user-defined threshold fraction value. Insets show a sample image frame (NSR=0.07) binarized according to two different threshold fractions (0.3 and 0.7). By eye, both appear reasonable, so a user might reasonably choose any value between 0.3 and 0.7, but the error varies substantially over that range, reaching a minimum value near 0.3% at threshold 0.45. The sensitivity of CST to threshold is a major limitation. All other reported results were produced using a threshold of 0.5.

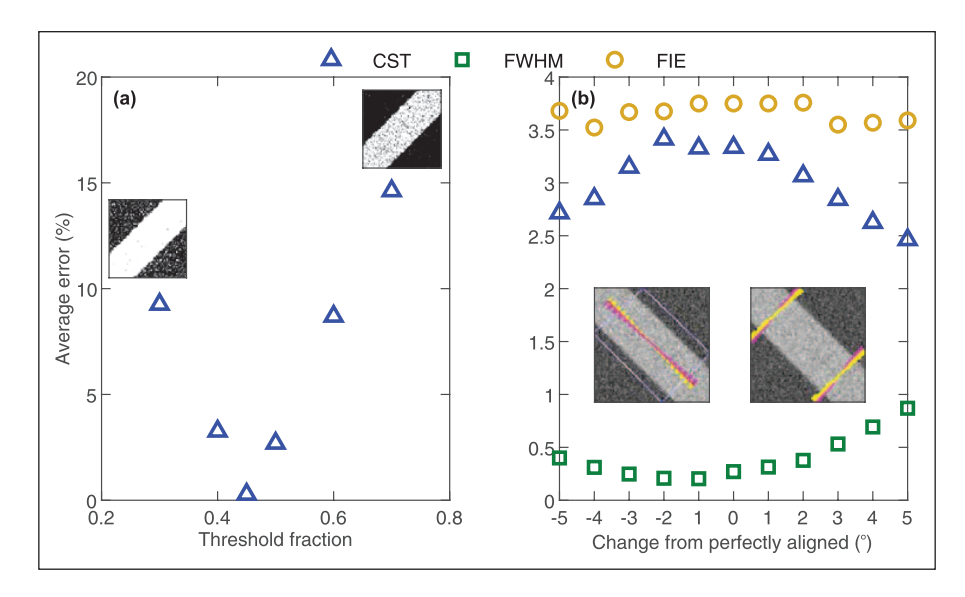


Figure 4. Variation in average error with user-selected (a) threshold fraction and (b) centerline or end cap angle with respect to a perfectly aligned orientation, where 0° corresponds to centerline and end caps that are parallel and perpendicular, respectively, to the vessel.

Figure 4(b) shows the variation of the average error with centerline orientation for CST and FWHM and with end cap orientation for FIE. The insets show centerlines and end caps whose orientation differs by as much as 5° from being perfectly aligned (parallel to the vessel for the centerline and perpendicular to the vessel for the end caps). We varied the orientation of the centerline and end caps by as much as $\pm 5^{\circ}$ from an orientation perfectly parallel or perpendicular to the vessel. The change in average error with the orientation of the centerline or end caps was marginal for all three algorithms. The errors for CST and FWHM varied from 2.4% to 3.4% and from 0.2% to 0.8%, respectively. The error for FIE varied from 3.5% to 3.7%. Results depended weakly on the random noise in each frame.

Validating IQR metric

To test the IQR metric and its ability to quantify amplitudes in signals containing multiple frequency components, such as those containing both slow vasomotion and cardiac pulsations, we applied the IQR metric to synthetic signals containing three frequencies (equation (2)) and Gaussian noise with standard deviation either 1 or 2 (on a 0–1 brightness scale). The signals were sampled at 30 Hz and bandpass filtered with the cutoff frequencies listed in Table 1, which also shows the true and measured amplitudes. In cases with no or little noise, the IQR metric worked well, producing errors <3%. The IQR metric produced a larger error (34%) when the standard deviation of the noise is twice the amplitude in the cardiac frequency band.

Comparing pulsatility metrics

We compare the amplitudes obtained using the PA and IQR metrics in Figure 5, which was produced with synthetic data and a 2-pixel pulsation amplitude. Figure 5(a) shows the distribution of diameter measurements with a box plot, where the box illustrates the IQR. FIE and FWHM produce diameter measurements whose IQR matches ground-truth closely; CST is less accurate. Figure 5(b) compares the ground-truth and PA waveforms. PA measurements from FIE and FWHM track the true values much more closely than do those from CST.

Figure 5(c) shows the variation of pulsatility error with pulsation amplitude in synthetic data with NSR of 0.07. The error increases substantially for amplitudes <0.4 pixel but changes little for amplitudes of 1 pixel or larger. Specifically, for an amplitude of 0.2 pixel, we find errors of 88.4%, 41.1%, and 28.7% for FIE, CST, and FWHM, respectively, when quantified using IQR, and 92.9%, 79.5%, and 75.6%, respectively, when quantified using PA. For amplitudes exceeding 0.2 pixel, pulsatility errors are smaller with FWHM and FIE than with CST. For an amplitude of 0.2 pixel, none of the algorithms accurately capture pulsations. Trends in errors quantified with IQR and PA are broadly similar, suggesting that both metrics are useful in the presence of low to moderate noise.

Figure 5(d) compares pulsatility error obtained using the IQR and PA approaches for varying NSR. All three algorithms predict similar pulsatility errors from the IQR and PA approaches when the NSR is \leq 1. However, at higher NSR values, IQR, and PA differ more significantly for CST and FWHM.

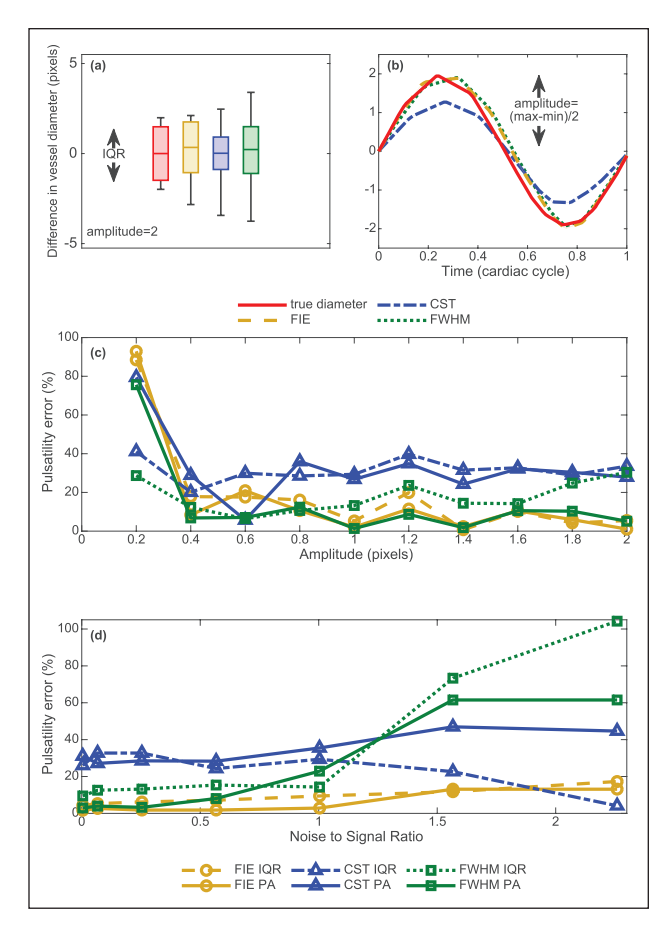


Figure 5. (a) Box plots showing the distribution of diameter measurements and illustrating the interquartile range (IQR). The bottom and top edges of each box indicate the 25th and 75th percentiles of diameter fluctuation; the IQR is the box height. The whiskers extend to the minimum and maximum diameter fluctuations, and the middle line is the median. (b) Ground-truth and PA vessel diameter waveform, where lines indicate mean values and shaded regions indicate standard error of the mean. Results in (a, b) are for synthetic data with two-pixel pulsation amplitude. (c) Pulsatility error for different pulsation amplitudes quantified with IQR and PA. (d) Pulsatility error for varying noise-to-signal ratios from the IQR and PA approaches. The results from the two approaches are similar for low to moderate levels of noise. PA: phase-averaging.

Discussion

This study used synthetic and experimental images to test the accuracy of three vessel diameter measurement algorithms. We introduced a new algorithm (FIE) and found it to be more robust to noise and perpendicular brightness gradients than two previously used algorithms (CST and FWHM). 5,9,19,24,28 The FIE algorithm also quantifies vessel pulsatility most accurately. We found that FWHM most accurately measured absolute vessel diameters for images with NSR below 0.5 and sufficient contrast between the vessel and its surroundings, and we introduced a modification to FWHM that allows it to perform well in high noise/low contrast situations. The modified FWHM algorithm measured

the absolute vessel diameter most accurately, while FIE most accurately measured changes in vessel diameter, like pulsatility. CST is sensitive to the user-defined threshold, underestimating the diameter when the threshold is 0.5 in the synthetic data but overestimating the diameter when the chosen threshold is below 0.45 (see Figure 4(a)). The differences between the algorithm's performance increase with increasing noise. The IQR metric is a reasonable alternative to PA for estimating pulsation amplitude, though it does not provide other information about the waveform. We summarize the advantages and disadvantages of the algorithms in Table 2.

FIE overestimates the vessel diameter due to the discretization of the vessel edge, resulting in a maximum error of 2 pixels, one from either side of the vessel. Thus, the maximum systematic error in FIE is a function of the image resolution, can be calculated quite precisely, and can be reduced by increasing the image resolution. For the synthetic data in this work, with a 40-pixel diameter, this corresponds to an average error of 5%, and the error we measure from FIE is always smaller than this limit in low and moderate noise cases. In many situations, the change in vessel diameter matters more than the absolute diameter, and in that case, consistently overestimating the vessel width by a pixel or two would not affect the results, which is why FIE has relatively low pulsatility error.

Whether FIE or the modified FWHM is the best algorithm to use to measure vessel diameter depends on the goals (is absolute or change in vessel diameter more important) and the particular challenges of the imaging data. For example, there are cases where large gaps in the vessel edges detected by FIE cause it to fail, but FWHM does not, since it averages over the entire ROI. On the other hand, there are also cases where changes in background image intensity between sides of the vessel, or the presence of an adjacent vessel, cause FWHM to fail where FIE does not. Sometimes it is obvious which approach is better just from inspecting the diameter measurements, but in other cases, visualizing the measured diameters overlayed on the original images is the best approach to determine which is best.

All three algorithms were robust to translation in the direction perpendicular to the vessel in the synthetic data with perfectly straight edges, but this should not be interpreted as an indication that vessel translation would never result in error. In cases where the vessel diameter varies along its axis, translations in the direction parallel to the vessel would result in pulsatility error for all three algorithms.

There are a few limitations to the synthetic data used in this study to test the algorithms' performance. The generated synthetic data included only a single frequency, while experimental recordings may consist of multiple, varying frequencies, such as those associated with slow vasomotion, respiratory oscillations, and cardiac pulsations. The synthetic images had dimensions $100 \times 100\,\mathrm{pixels}$, which is smaller than what is typical in two-photon microscopy, though comparable to other imaging modalities. Two-photon microscopy typically has a narrow focal

Table 2. Advantages and disadvantages of vessel diameter measurement algorithms.

Algorithm	Advantage	Disadvantage	
FIE	 Robust to high NSR and lighting artifacts Well-suited for pulsatility analysis Provides visual feedback of the results 	 Sensitive to images with discontinuous edges Performs worst at capturing small amplitude (0.2 pixel) vessel pulsation 	
VD	Provides visual feedback of the results	 Sensitive to the choice of threshold fraction Generally results in the highest RMS, average, and pulsatility error 	
FWHM	 Requires minimal user input and processing time Lowest average errors when applied to low NSR images (or when using the modified version) 	 Does not perform well for images with high NSR and brightness gradients perpendicular to the vessel No visual feedback of the results 	

NSR: noise-to-signal ratio.

plane, so vessel motion in and out of the plane can change the apparent vessel diameter, but we did not investigate this potential source of error. The algorithms discussed here are unsuitable for measuring the diameter of penetrating vessels, which typically extend perpendicular to the imaging plane and appear as circular cross sections. However, FIE and FWHM have been adapted for measuring the diameter of penetrating vessels.^{29,30}

Accurate measurement of pial artery diameter is essential as changes in the vessel's size are correlated with alterations in regional cerebral blood flow, which in turn affects the brain function and health.³¹ Furthermore, accurate quantification of vessel dynamics, or pulsatility, is critical, since vessel pulsatility has been shown to impact the brain's waste clearance mechanisms. Mestre et al. found that vessel pulsatility is a primary driver of CSF flow through pial PVSs, which is critical for clearance of amyloid- β and other solutes.⁹ Accordingly, vessel pulsatility has been used in several recent simulations to drive CSF flow,^{7,32} and their predictions can be accurate only if the prescribed pulsatility comes from accurate experimental measurements.

Conclusion

We compared three techniques to measure vessel diameter from images and two approaches to quantify pulsatility. The new approaches we presented for diameter measurement (FIE) and pulsatility analysis (IQR) are effective. A modified version of FWHM captures the absolute vessel diameter most accurately, whereas FIE outperforms FWHM when considering changes in vessel diameter, like pulsatility. The IQR approach quantifies vessel pulsatility as well as the previously used method, PA, without relying on information about cycle timing.

Acknowledgements

We gratefully acknowledge Yue Zhao's work incorporating the find image edges algorithm into the vessel-diameter-andpulsatility-analysis app, and Patrick Drew for helpful conversations regarding FWHM.

Author contributions

Aditya Ranjan, Devin T Wong: generated the synthetic data, performed the data analysis, and drafted the manuscript. Kimberly A S Boster: developed the find image edges (FIE) algorithm and interquartile range (IQR) approach. Kimberly A S Boster and Douglas H Kelley: study supervision and revision of the manuscript. Qinwen Huang and Hashmat Ghanizada: experimental data acquisition. Maiken Nedergaard: supervision of the experimental data acquisition and revision of the manuscript.

Funding

The authors disclosed receipt of the following financial support for the research, authorship, and/or publication of this article: All authors acknowledge support from the U.S. NIH National Center for Complementary and Integrative Health (R01AT012312), the BRAIN Initiative of the US National Institutes of Health (U19NS128613), and from the U.S. Army (MURI W911NF1910280).

Declaration of conflicting interests

The authors declared no potential conflicts of interest with respect to the research, authorship, and/or publication of this article.

Ethical considerations

Not applicable.

Consent to participate

Not applicable.

Consent for publication

Not applicable.

ORCID iDs

Aditya Ranjan https://orcid.org/0000-0001-9769-7374

Devin T Wong https://orcid.org/0009-0003-4867-4872

Qinwen Huang https://orcid.org/0009-0005-8106-3410

Hashmat Ghanizada https://orcid.org/0000-0001-7954-8519

Douglas H Kelley https://orcid.org/0000-0001-9658-2954 Kimberly A S Boster https://orcid.org/0000-0001-5178-128X

Data availability statement

All algorithms and data used in this paper are available for use. The app version of the find image edges (FIE) algorithm is available on GitHub (https://github.com/yzhaoinuw/vesseldiameter-and-pulsatility-analysis-app). The cross-section threshold (CST) algorithm is available on Zenodo (https://doi.org/10.5281/zenodo.8165799, in the PTV ToolBox folder). The original version of full width at half maximum (FWHM) is available on GitHub (https://github.com/DrewLab/Surface-Vessel-FWHM-Diameter), and the modified version of FWHM (Modified_FWHM) and an example synthetic data set are available on GitHub (https://github.com/aditya22-FluidLab/Modified_FWHM). The experimental data are available on DANDI (https://dandiarchive.org/dandiset/001366).

Supplemental material

Supplemental material for this article is available online.

References

- Bollmann S, Mattern H, Bernier M, et al. Imaging of the pial arterial vasculature of the human brain in vivo using high-resolution 7T time-of-flight angiography. *Elife* 2022; 11: e71186.
- Sekiguchi Y, Takuwa H, Kawaguchi H, et al. Pial arteries respond earlier than penetrating arterioles to neural activation in the somatosensory cortex in awake mice exposed to chronic hypoxia: an additional mechanism to proximal integration signaling? *J Cereb Blood Flow Metab* 2014; 34(11): 1761–1770.
- 3. Chen HC, Patel V, Wiek J, et al. Vessel diameter changes during the cardiac cycle. *Eye* 1994; 8(1): 97–103.
- van Veluw SJ, Hou SS, Calvo-Rodriguez M, et al. Vasomotion as a driving force for paravascular clearance in the awake mouse brain. *Neuron* 2020; 105(3): 549–561.
- Holstein-Rønsbo S, Gan Y, Giannetto MJ, et al. Glymphatic influx and clearance are accelerated by neurovascular coupling. *Nat Neurosci* 2023; 26(6): 1042–1053.
- Institoris A, Vandal M, Peringod G, et al. Astrocytes amplify neurovascular coupling to sustained activation of neocortex in awake mice. *Nat Commun* 2022; 13(1): 7872.
- 7. Kedarasetti RT, Turner KL, Echagarruga C, et al. Functional hyperemia drives fluid exchange in the paravascular space. *Fluids Barriers CNS* 2020; 17(1): 52.
- 8. Vora YY, Suarez-Almazor M, Steinke DE, et al. Role of transcranial Doppler monitoring in the diagnosis of cerebral vasospasm after subarachnoid hemorrhage. *Neurosurgery* 1999; 44(6): 1237–1247.
- 9. Mestre H, Tithof J, Du T, et al. Flow of cerebrospinal fluid is driven by arterial pulsations and is reduced in hypertension. *Nat Commun* 2018; 9(1): 4878.
- Bojarskaite L, Bjørnstad DM, Pettersen KH, et al. Astrocytic Ca²⁺ signaling is reduced during sleep and is involved in the regulation of slow wave sleep. *Nat Commun* 2020; 11: 3240.
- 11. Kelley DH and Thomas JH. Cerebrospinal fluid flow. *Annu Rev Fluid Mech* 2023; 55: 237–264.
- Bohr T, Hjorth PG, Holst SC, et al. The glymphatic system: current understanding and modeling. *iScience* 2022; 25(9): 104987.

- Lee J, Jirapatnakul AC, Reeves AP, et al. Vessel diameter measurement from intravital microscopy. *Ann Biomed Eng* 2009; 37: 913–926.
- Kolkman GM, Klaessens JH, Hondebrink E, et al. Photoacoustic determination of blood vessel diameter. *Phys Med Biol* 2004; 49(20): 4745.
- Fischer MJM, Uchida S and Messlinger K. Measurement of meningeal blood vessel diameter in vivo with a plug-in for ImageJ. *Microvasc Res* 2010; 80(2): 258–266.
- Baran U, Li Y and Wang RK. Vasodynamics of pial and penetrating arterioles in relation to arteriolo-arteriolar anastomosis after focal stroke. *Neurophotonics* 2015; 2(2): 025006.
- Will C, Messlinger K and Fischer MJM. Vessel diameter measurements at the medullary brainstem in vivo as an index of trigeminal activity. *Brain Res* 2016; 1632: 51–57.
- Glück C, Zhou Q, Droux J, et al. Pia-flow: deciphering hemodynamic maps of the pial vascular connectome and its response to arterial occlusion. *Proc Natl Acad Sci U S A* 2024; 121(28): e2402624121.
- Huo BX, Gao YR and Drew PJ. Quantitative separation of arterial and venous cerebral blood volume increases during voluntary locomotion. *Neuroimage* 2015; 105: 369–379.
- Kim D, Gan Y, Nedergaard M, et al. Image analysis techniques for in vivo quantification of cerebrospinal fluid flow. *Exp Fluids* 2023; 64(11): 181.
- Canny J. A computational approach to edge detection. *IEEE Trans Pattern Anal Mach Intell* 1986; 8(6): 679–698.
- Lim JS. Two-dimensional signal and image processing. Englewood Cliffs, NJ: Prentice-Hall, 1990.
- Parker JR. Algorithms for image processing and computer vision. Hoboken, NJ: Wiley, 2010.
- Drew PJ, Shih AY and Kleinfeld D. Fluctuating and sensory-induced vasodynamics in rodent cortex extend arteriole capacity. *Proc Natl Acad Sci U S A* 2011; 108(20): 8473–8478.
- Percie du Sert N, Hurst V, Ahluwalia A, et al. The ARRIVE guidelines 2.0: updated guidelines for reporting animal research. *J Cereb Blood Flow Metab* 2020; 40(9): 1769–1777.
- Boster KAS, Cai S, Ladron-de-Guevara A, et al. Data from "Artificial intelligence velocimetry reveals in vivo flow rates, pressure gradients, and shear stresses in murine perivascular flows". Zenodo 2023. [Data set]. DOI: 10.5281/ zenodo.7723381.
- Boster KAS, Cai S, Ladrón-de Guevara A, et al. Artificial intelligence velocimetry reveals in vivo flow rates, pressure gradients, and shear stresses in murine perivascular flows. *Proc Natl Acad Sci U S A* 2023; 120(14): e2217744120.
- 28. Turner KL, Gheres KW, Proctor EA, et al. Neurovascular coupling and bilateral connectivity during NREM and REM sleep. *Elife* 2020; 9: e62071.
- Gan Y, Holstein-Rønsbo S, Nedergaard M, et al. Perivascular pumping of cerebrospinal fluid in the brain with a valve mechanism. *J R Soc Interface* 2023; 20(206): 20230288.
- 30. Gao YR and Drew PJ. Determination of vessel cross-sectional area by thresholding in Radon space. *J Cereb Blood Flow Metab* 2014; 34(7): 1180–1187.
- Rosenblum WI and Kontos HA. The importance and relevance of studies of the pial microcirculation. *Stroke* 1974; 5(4): 425–428.
- Bojarskaite L, Vallet A, Bjørnstad DM, et al. Sleep cycledependent vascular dynamics in male mice and the predicted effects on perivascular cerebrospinal fluid flow and solute transport. *Nat Commun* 2023; 14(1): 953.